Smart Materials and Structures

PURPOSE-LED PUBLISHING™

PAPER · **OPEN ACCESS**

Boron nitride-based shape memory polymers for spatially targeted ultrasound actuation

To cite this article: Jiaxin Xi *et al* 2025 *Smart Mater. Struct.* **34** 075018

OPEN ACCESS
IOP Publishing
Smart Materials and Structures
Smart Mater. Struct. **34** (2025) 075018 (9pp)
https://doi.org/10.1088/1361-665X/adeb1c

Boron nitride-based shape memory polymers for spatially targeted ultrasound actuation

Jiaxin Xi[1], **David L Safranski**[2,3], **Reza Mirzaeifar**[1] **and Shima Shahab**[1,*]

[1] Department of Mechanical Engineering, Virginia Tech, Blacksburg, VA 24061, United States of America
[2] Enovis Foot & Ankle, Atlanta, GA 30318, United States of America
[3] School of Materials Science and Engineering, Georgia Institute of Technology, Atlanta, GA 30332, United States of America

E-mail: sshahab@vt.edu

Received 16 April 2025, revised 13 June 2025
Accepted for publication 2 July 2025
Published 10 July 2025

Abstract

Focused ultrasound (FUS) presents unique advantages for noninvasive localized heating, crucial for controlled shape recovery in shape memory polymers (SMPs), especially in biomedical applications. To enhance FUS-driven actuation efficiency, we propose boron nitride (BN)-infused SMP composites (SMPCs) tailored for targeted biomedical interventions. Using tert-butyl acrylate (tBA) and di(ethylene glycol) dimethacrylate as base materials, we integrated BN fillers at varying concentrations (1, 5, and 10 wt.%). A thorough characterization was carried out, including dynamic mechanical analysis, scanning electron microscopy, uniaxial tensile testing, and swelling study. These results show that increasing the BN content improves shape recovery efficiency significantly. Specifically, the 10 wt.% BN composites outperformed plain SMP in terms of shape recovery ratio when activated with FUS, and the highest shape recovery ratio can achieve 75%. However, higher BN content decreases crosslinking density and stiffness, as shown by a lower Young's modulus and glass transition temperature. This study demonstrates the promise of BN-infused SMPCs for advanced applications in biomedical application, where noninvasive spatiotemporal actuation of SMPs is required.

Supplementary material for this article is available online

Keywords: polymers, ultrasound, shape memory polymer, biomedical applications, boron nitride, focused ultrasound

1. Introduction

Shape memory polymers (SMPs) have garnered extensive attention in biomedical fields due to their unique ability to return to a pre-determined shape when exposed to external stimuli such as heat, solvents, magnetic fields, and focused ultrasound (FUS) fields [1–6]. SMPs are lightweight, cost-effective, and versatile [7–9], which makes them ideal candidates for various applications, including soft actuators and robotics [10, 11], switchable adhesive for transfer printing [12–15], aerospace [16], tissue engineering [17–19], and biomedicine [20–23]. Based on their stimulus, SMPs can be classified into chemo-responsive, thermo-responsive, and photo-responsive categories [24–27]. Among these, thermo-responsive SMPs are most widely used, due to their excellent shape memory properties and the ability to precisely tune their switching temperatures. Thermo-responsive SMPs are typically activated by heat, which alters the material's

* Author to whom any correspondence should be addressed.

stiffness and molecular motion above a transition temperature, enabling shape recovery [28]. Compared to traditional direct heating methods, FUS represents a novel and promising external stimulus with superior capabilities for noninvasively achieving shape recovery. FUS induces localized heating, activating intermediate states in the material and enabling controlled shape change [29–31]. The mechanism involves focusing ultrasound into a small, targeted area on the scale of millimeters, resulting in selective and precise heating of the medium, which leads to partial or complete shape recovery [30, 32]. Recently, FUS-actuated SMPs have been reported for biomedical applications, such as stents, tissue scaffolds, drug delivery systems, and orthopedic devices [33–35]. Despite these advancements, developing efficient SMPs for remote actuation remains a challenge, especially when it comes to achieving full shape recovery within a few seconds [30, 36, 37]. Addressing these challenges is essential for advancing SMPs for high-performance and practical uses.

Acrylate-based SMPs, with their biocompatibility [38, 39], offer a promising candidate for biomedical applications. To address the issue of recovery triggered by FUS, our group previously investigated the influences of the chemical composition on FUS-induced shape recovery in SMPs [37]. By synthesizing SMPs using tert-butyl acrylate (tBA) as monomer and di(ethylene glycol) dimethacrylate (DEGMA) as crosslinker, we optimized the monomer-to-crosslinker ratio to achieve a shape recovery ratio of approximately 20% after 20 s of continuous ultrasonic exposure. Additionally, we explored the benefits of pre-immersion in water for hydrophilic SMPs, which significantly improved shape recovery efficiency under FUS while reducing energy consumption [40]. Peng *et al* [41] incorporated polystyrene into SMP networks to enhance the recovery ratio, achieving nearly 100% shape recovery within 2 s under direct heating. Due to the increased viscoelasticity from polystyrene, they also suggested that its addition could enhance the material's recovery ability after FUS exposure. Despite these advancements, the performance of these SMPs is still constrained by low recovery stress and slower recovery times.

Incorporating fillers into SMPs is a widely used strategy to enhance their mechanical and thermal properties [42]. Fillers such as graphene sheets [43], hydroxyapatite nanoparticles [44], carbon nanotubes (CNTs) [45] and boron nitride (BN) [46] have been shown to improve stiffness, recovery stress, and thermal conductivity. Chen *et al* [47] demonstrated that reduced graphene oxide (GO) nanofillers enhanced thermal conductivity and reduced recovery times in epoxy-based SMPs. Li *et al* [48] Integrated GO into liquid crystalline polyurethane (LCPU) composites, resulting in a 1.78-fold increase in tensile strength compared to neat LCPU, alongside improved shape recovery speed. Qu *et al* [49] Incorporated CNTs into polycaprolactone and thermoplastic polyurethane fibers, which have enhanced both shape memory and strain sensing performance, demonstrating the potential for multifunctional applications. Among these fillers, BN is particularly noteworthy due to its exceptional thermal conductivity ($\sim$400 W(m·K)$^{-1}$), high hardness, and large surface area [50, 51]. More importantly, several reports have shown that BN exhibits favorable biocompatibility both *in vitro* and *in vivo* [52–55]. Thus, BN not only acts as a rigid phase to improve stiffness but also accelerates heat transfer, enabling faster and more efficient shape recovery [56, 57], showing great potential for biomedical SMP composites (SMPCs). However, to the best of our knowledge, no study has systematically investigated the integration of BN into SMPs specifically for actuation under FUS. This work addresses this knowledge gap by developing and characterizing BN-infused acrylate-based SMPCs tailored for FUS-triggered applications. The synergy between BN and FUS lies in BN's high thermal conductivity, which enhances the localized temperature rise generated by FUS, enabling faster and more efficient shape recovery. This capability is particularly critical for biomedical use, where precise, minimally invasive, and rapid actuation is required. To the best of our knowledge, this is the first study to demonstrate and quantify the role of BN fillers in enhancing shape recovery performance under FUS stimulation.

In this study, we synthesized BN-infused SMPCs and systematically characterized for their chemical structures, transition temperatures, and mechanical properties, as well as shape recovery performance under ultrasound. This work presents a benchmark strategy for developing next-generation SMP composites optimized for remote, high-speed biomedical actuation, laying the groundwork for future FUS-responsive smart materials.

2. Materials and methods

2.1. Sample preparation

tBA, DEGMA, BN, and the photoinitiator 2,2-dimethoxy-2-phenyl-acetophenone were purchased from Sigma-Aldrich and used as received without further modification.

In a typical experiment, tBA (monomer) and DEGMA (crosslinker) were first mixed at a weight ratio of 85:15, followed by adding 1 wt.% photoinitiator into the solution. The solution was then fully stirred for 20 min. BN was then added to the prepared tBA-co-DEGMA (tD) solution at weight ratios of 1:99, 5:95 and 10:90, and the mixtures were further homogenized using an ultrasonic mixer for another 30 min.

Two types of shaping methods were studied in this work. In the first method, the prepared solution was injected into a mold composed of two glass slides separated by 1 or 2 mm silicone rubber spacers, with the glass slides pre-coated with Rain-X to facilitate mold release. The second type of shaping method utilized a soft mold. The silicone material (Ecoflex 00-50, Macungie, PA, USA) was used to fabricate molds by casting and curing the material in 3D-printed PLA molds (Prusa i3 MK3, Prague, Czech Republic).

For both methods, the resultant solution was carefully poured into the respective molds to shape the target samples. The molds were then polymerized for 15 min using an 365 nm UV light (with a 100 W Blak-Ray B-100 AP High Intensity UV Lamp). After polymerization, the prepared samples were post-cured and dried in a fume hood for 24 h. The entire synthesis procedures are shown in figure 1.

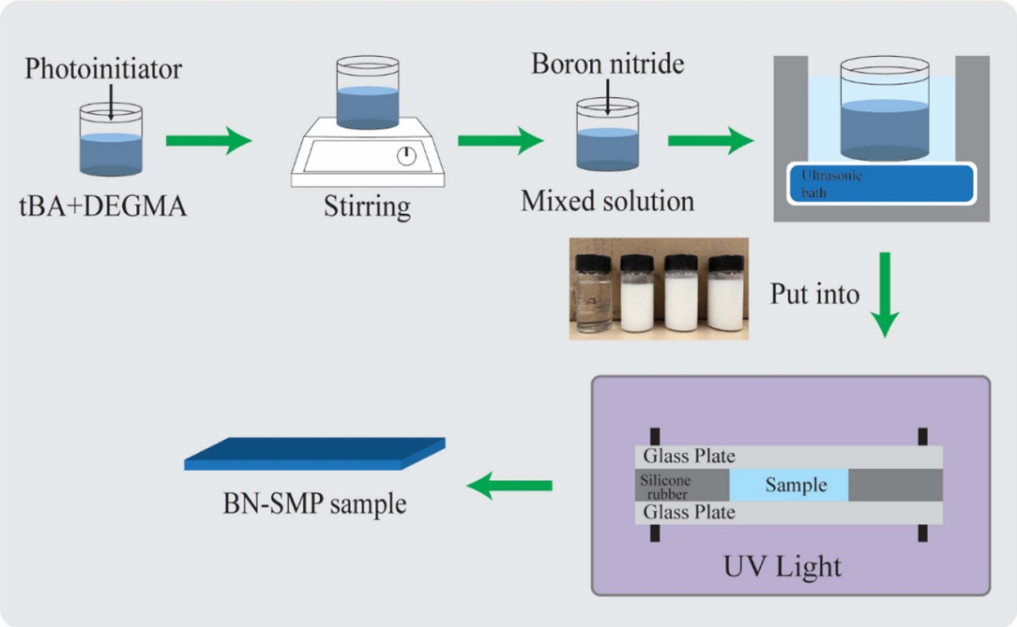

Figure 1. Schematic showing processing steps to prepare tD/BN composites.

2.2. SEM analysis of BN nanoparticles and TD/BN composite

Scanning electron microscopy (SEM, JEOL IT-500 h) with energy dispersive x-ray spectroscopy (EDS, Oxford Instruments, AZtecLive Automated Microanalysis System) was used to investigate the dispersion of BN within the composites under 5 kV accelerating voltage. Prior to characterization, the fracture surfaces of all samples were coated with a 7.0 nm layer of platinum/lead, using a sputter coater. Field emission SEM (FESEM, FEI Quanta 600 FEG) was employed to analyze the surface morphology and determine particle size of BN nanoparticles.

2.3. Dynamic mechanical analysis

Dynamic Mechanical Analysis was performed to measure the temperature-dependent storage modulus, loss modulus, and tan delta, following ASTM D4065 standard [58]. The test was conducted in dynamic mode using a TA-Q800 DMA (TA Instruments) at a frequency of 1 Hz. Specimens with dimensions of 20 mm × 5 mm × 1 mm were heated to 120 °C at a rate of 2 °C min^{-1}. The test was carried out under 0.1% dynamic strain, with a preload force of 0.001 N and a force track of 150%. To ensure repeatability, each composition was tested at least three times ($n = 3$).

2.4. Tensile testing

The mechanical properties of each sample were measured by a Tension/Compression Testing System (Instron 3340 Universal Testing System), following the standard ASTM D638 [59] and ASTM D3039 [60]. Tensile specimens of dog-bone shape (Type I) with thickness of 3.2 mm were produced in accordance with ASTM D638 and tested with a crosshead speed of 10 mm min^{-1} at room temperature (i.e. 25 °C).

2.5. Cross-linking density determination using swelling experiments

A swelling test was conducted to determine the crosslinking density of tD and tD/BN. Crosslinked polymers, although insoluble in solvents, can exhibit a degree of swelling, which is related to the polymer's crosslink density. The Flory–Rehner theory [61] provides a framework for analyzing the equilibrium swelling behavior. The crosslink density (γ, mol cm^{-3}) is calculated using the following equation:

$$\gamma = \frac{\rho_p}{M_c} = -\frac{V_s \ln(1-\emptyset_p) + \emptyset_p + \chi\phi_p^2}{V_s \emptyset_p^{\frac{1}{3}}} \tag{1}$$

here, ρ_p is the polymer density before swelling, V_s is the solvent molar volume ($V_s = 73.4\ \text{cm}^3\,\text{mol}^{-1}$), and χ is the Flory–Huggins interaction parameter, which quantifies the interaction strength between the polymer and the solvent. It is noted that for specific systems, such as acrylate-base polymer system in acetone, precise values of χ are not readily available in the provided sources. However, acetone is generally considered a good solvent for many acrylate-based polymers, suggesting that χ is likely less than 0.5, indicating favorable mixing and solubility. Here, we assume χ is 0.5. Additionally, $\emptyset_p$ corresponds to the polymer's volume fraction at swelling equilibrium, and can be calculated as follows:

$$\phi_p = \frac{\frac{W_0}{\rho_p}}{(W_{sw} - W_o)/\rho_s + W_0/\rho_p} \tag{2}$$

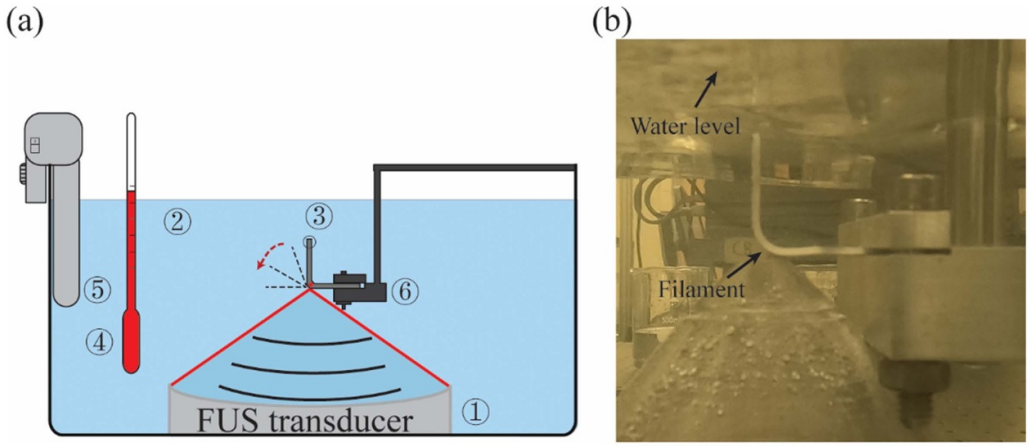

Figure 2. (a) Illustration of the experimental setup; ① FUS transducer placed on the bottom of the tank; ② custom water bath; ③ filament; ④ thermometer; ⑤ immersion tank heater; ⑥ sample holder. (b) Experimental HIFU setup.

where ρ_s (=0.7857 g cm^{-3}) is the density of acetone, W_0 is sample's initial weight, and W_{sw} is the swelling equilibrium weight.

In this study, crosslink density was determined using the equilibrium swelling method, following a standard ASTM F2214 [62]. Each sample, approximately 10 mm × 10 mm × 10 mm and weighing around 1 g, was immersed in 15 ml acetone in glass tubes. Samples were periodically removed, and the surface solvent was blotted using filter paper. Equilibrium swelling was considered achieved when the mass variation between consecutive measurements was within 5 mg. From the equilibrium swelling data, the crosslink density of was calculated.

2.6. FUS system configuration and shape memory testing and FUS thermal effect

Figure 2 illustrates the configuration of the FUS system, comprising two main components: a FUS transducer and a sample-holder module. The H-104-4A SONIC Concepts FUS transducer was positioned at the bottom of a water-filled tank, with the water temperature maintained at 37 °C to simulate body temperature. The ultrasound frequency was set to 500 kHz. Recovery tests were conducted on flat film specimens measuring 50 mm × 5 mm × 2 mm.

First of all, the specimen was first heated to 75 °C in an oven for 10 min and subsequently folded into an L-shape ($\theta_0 = 90°$) for another 10 min. The folded specimen was air-cooled while clamped, and the clamps were then released. Afterwards, to verify that shape recovery was specifically triggered by FUS stimulation, a control experiment was conducted. In this setup, bent samples were submerged in a 37 °C water bath, but without applying ultrasound. After then, FUS was applied to actuate the specimen for 10 min. It is noted that the sample bend had to be located on the focal point of the FUS transducer, as shown in figure 2.

During the recovery process, a digital camera recorded the specimen's shape evolution. Kenova (version 0.9.5, an open-source project) [63] was used to process the recorded video and output recovery angles (θ_r) at fixed intervals. This approach allowed us to capture both the transient shape evolution and final deformation state of the SMP composites under FUS activation. The recovery ratio (R_r) was defined as the ratio of the recovered angle (θ_r) to the initial folding angle (θ_0). To minimize experimental errors, six runs for each sample were conducted ($n = 6$).

2.7. FUS thermal effect

Thermal variations in the polymer filament exposed to FUS were measured using a Teledyne FLIR A50 thermal imaging camera. Due to the limitations of thermal cameras, which are unsuitable for analyzing submerged objects, the sample was suspended such that its lower surface was submerged in water while the upper surface remained exposed to air. Ultrasonic actuation was applied continuously for 60 s, with thermal measurements extending to 180 s to capture the complete thermal history. The data was analyzed using FLIR Tools software.

3. Results and discussion

The morphology and structure of the BN used in this study were examined using FESEM to assess particle shape, size, and dispersion (see section 2.2 for details). SEM micrographs (figure 3) indicated that BN particles predominantly exhibited an irregular flake-like morphology. SEM micrographs of multiple samples were analyzed using ImageJ software, followed by statistical analysis of particle sizes. The results show that the size distribution ranges from 100 to 400 nm and an average size of 201 ± 72 nm. The average thickness of the platelets was estimated by measuring 20 particles oriented out-of-plane. This platelet-like structure aligns with previously reported morphologies for hexagonal BN fillers [64].

The SEM analysis of composite samples containing 1, 5, and 10 wt.% BN revealed a homogeneous dispersion of BN platelets within the tD matrix at lower concentrations (1 and 5 wt.%), as shown in figures 4(a) and (c). However, at a higher concentration of 10 wt.% BN, partial agglomeration of BN

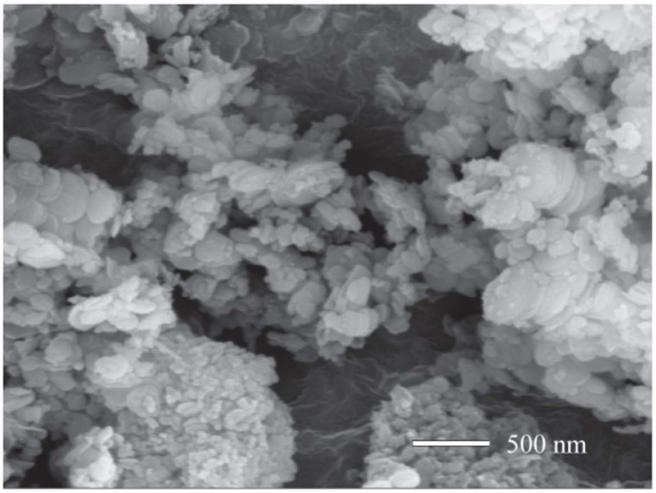

Figure 3. FE-SEM image of BN powder.

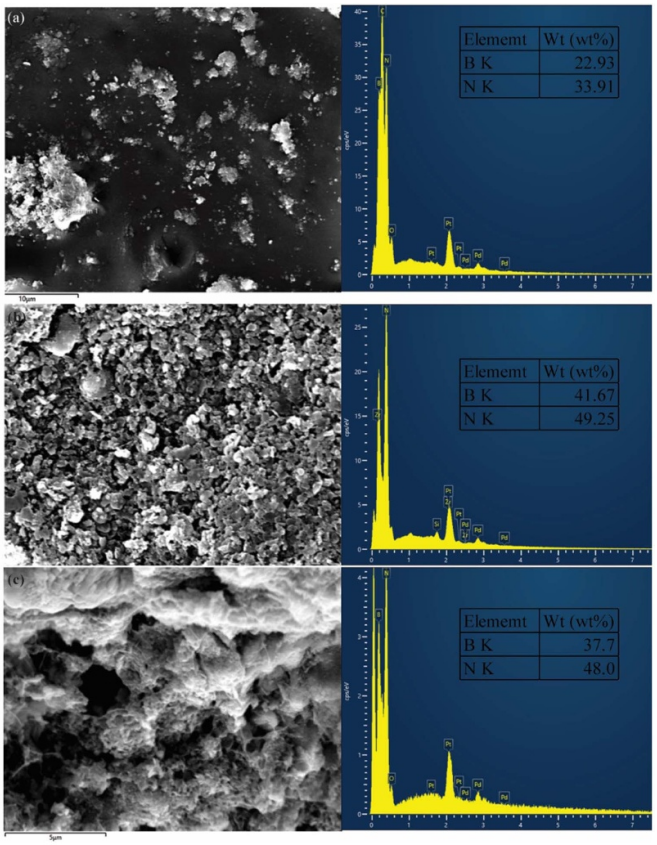

Figure 4. SEM images (a), (c), (e) and EDS graphs (b), (d), (f) of (a) 1, (c) 5, and (e) 10 wt.% loadings of BN in tD.

platelets was observed, likely due to the poor wetting and high surface energy of the nanoparticles, leading to clustering within the matrix. Such agglomeration can create stress concentration points, adversely affecting the mechanical integrity and thermal performance of the composite [65]. These findings align with previous studies indicating that higher filler loadings can lead to nanoparticle aggregation, which diminishes the reinforcing efficiency and overall performance of polymer nanocomposites [66]. Therefore, optimizing the filler content is essential to balance improved properties with the challenges of nanoparticle dispersion.

DMA curves obtained to examine viscoelastic behaviors such as storage modulus (E'), $\tan\delta$, and T_g of each tD and tD/BN composites are shown in figure 5(a). The T_g values were determined to be approximately 82 °C for tD, 79 °C for tD/BN_1, 74 °C for tD/BN_5, and 70 °C for tD/BN_10. Those T_g ranges are significantly higher than body temperature (∼37 °C), ensuring that the materials remain in their temporarily fixed shapes under aqueous and body-temperature conditions prior to FUS activation. Figure 5(a) presents that a notable reduction in T_g was observed with increasing BN content. The overall transition temperature can be adjusted by incorporation fillers, which enhances the thermal conductivity of SMPCs. As a result, the characteristic segments of these SMPCs with fillers respond more quickly to the same heat input compared to SMPs without fillers. Consequently, the addition of fillers leads to a reduction in the transition temperature of the composites [67]. This behavior is attributed to the partial inhibition of crosslinking caused by BN, which introduces steric hindrance and limits monomer mobility during curing.

Uniaxial tensile tests on dog-bone-shaped specimens further confirmed the mechanical impact of BN incorporation. The Young's modulus decreased progressively with increasing BN content, measured as 1.490, 0.815, 0.677, and 0.562 GPa for tD, tD/BN_1, tD/BN_5, and tD/BN_10, respectively (figure 5(b)). From a biomedical perspective, such reductions in mechanical performance, particularly at higher BN loadings, may limit the material's suitability for load bearing or structurally demanding implant applications. However, for applications where compliance and flexibility are desirable, such as soft tissue scaffolds, drug delivery systems, or minimally invasive actuators, this trade-off could be acceptable [68].

The possible reasons for mechanical response variation were be investigated as followed by cross-linking density determination using swelling experiments. It could be said to be the main reason for the decrease in crosslink densities [69, 70]. The crosslink density of tD and tD/BN composites was analyzed using DMA and swelling experiments. The rubbery plateau modulus, observed in figure 5(a), correlates with the degree of crosslinking in the composites. A higher rubbery plateau modulus indicates a denser crosslinked network, while a lower modulus reflects reduced crosslinking. The results show a clear trend of decreasing rubbery plateau modulus with increasing BN content, signifying a reduction in crosslink density. The crosslinking density of each sample also was measured using a swelling test. Table 1 summarizes the crosslink densities, revealing a progressive reduction with increasing BN content. Specifically, crosslink densities decreased by 9%, 31%, and 33% for 1, 5, and 10 wt.% BN, respectively.

The reduction in crosslink density can be attributed to the steric hindrance introduced by BN particles, which disrupts the polymerization and curing processes [64]. This effect can interfere with monomer mobility and crosslinking efficiency during curing. BN's high aspect ratio and surface

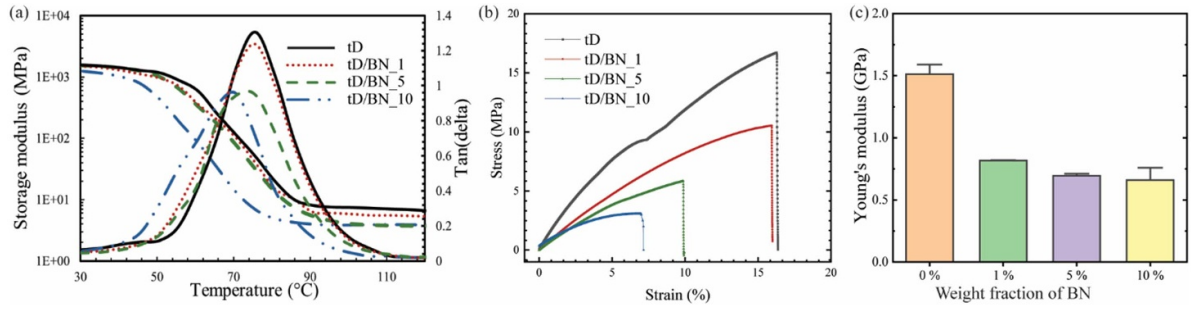

Figure 5. (a) DMA analysis; storage modulus versus temperature, and tan δ versus temperature. (b) Stress–strain curves and (c) Young's modulus of tD and tD/BN composites.

Table 1. Cross-linking density when swollen at equilibrium.

Sample	Density (g cm^{-3})	Cross-linking density ($\times 10^{-4}$ mol cm^{-3})
tD	0.922	1.345
tD/BN_1	0.9276	1.252
tD/BN_5	0.9492	1.022
tD/BN_10	0.9787	1.01

energy may also lead to localized aggregation, further limiting the formation of a tightly crosslinked network [64]. The decreased crosslink density has several implications for the material's mechanical and thermal properties. Reduced crosslinking leads to shorter molecular chains and looser networks, which increase local molecular mobility. This structural change results in composites with lower stiffness compared to the neat tD matrix. Similar observations have been reported for other nanofiller-infused polymer systems, where reduced crosslink density correlates with a decrease in tensile strength and Young's modulus [71].

The shape recovery process of the SMP is illustrated in section 2.6 and figure 2. First of all, control tests without FUS activation showed negligible shape change when samples were submerged in a 37 °C water bath, as shown in figure S1a in the supplementary information, while figure S1b shows FUS was a successful activation technique for SMPCs. This result confirms that the shape recovery observed in FUS-treated specimens was indeed induced by ultrasound. What is more, as depicted in figure 6(a), increasing the BN content in the SMP significantly enhanced the shape recovery ratio under FUS activation. Notably, the inclusion of 10 wt.% BN led to a remarkable improvement, achieving a shape recovery ratio of 75%. These findings underscore the efficacy of FUS as a powerful activation technique for SMPs, particularly due to its ability to generate a pronounced thermal effect localized to the target region.

The enhanced performance can be attributed to the synergistic interaction between FUS energy and the thermal conductivity of the BN-filled SMPCs. FUS generates localized heat through the absorption of acoustic energy by the polymer matrix. This energy arises from viscous shearing caused by the focused mechanical waves of FUS, which is then efficiently transferred as heat throughout the SMP matrix [72]. The high thermal conductivity of BN further accelerates this heat distribution, facilitating rapid and uniform shape recovery [73]. Additionally, the improved shape recovery ratio at higher BN content highlights the critical role of filler incorporation in enhancing the thermal response of SMPCs. However, achieving a balance between filler dispersion and content is crucial, as agglomeration at elevated BN concentrations could potentially hinder recovery efficiency.

To gain deeper insights into the shape recovery mechanism under FUS activation, thermal analysis of the samples was conducted. Figure 6(b) illustrates the equilibrium temperature achieved during FUS activation. As expected, the thermal effect was most pronounced in the sample containing the highest BN filler content, while tD exhibited the lowest temperature increase. It is noted that the equilibrium temperatures measured in section 2.6 do not reflect the actual temperatures during the shape recovery under FUS. It is because of the limitations of current thermal imaging setup (Teledyne FLIR A50), which is not suitable for measuring temperature changes in submerged environments; consequently, real-time thermal data could not be acquired [74]. The elevated thermal response in the BN-filled composites is attributed to the enhanced thermal conductivity of the BN platelets, which facilitated rapid and efficient heat transfer within the polymer matrix. The observed thermal behavior aligns with the viscoelastic nature of polymers. When subjected to ultrasonic waves, the polymer chains experience alternating stress due to forced vibrations. This dynamic action generates internal friction, causing energy dissipation. In viscoelastic materials, the energy absorbed from mechanical waves divides into two components: one part is released as heat, and the other is stored as elastic deformation within the polymer chains. The efficient conversion of ultrasonic energy into heat explains the temperature rise observed in the FUS-exposed samples. The generated heat raises the material's temperature above its activation temperature, triggering shape recovery. Therefore, the incorporation of BN allowed lower-level acoustic power to achieve the activation temperature, thereby minimizing the risk of internal damage to the polymer. These findings align with previous reports demonstrating the effectiveness of BN as a thermally conductive filler in polymer composites. Rybak *et al* [75] discussed the enhancement of thermal conductivity in SMPs through the incorporation of BN, highlighting its role in improving heat management in electrical insulation

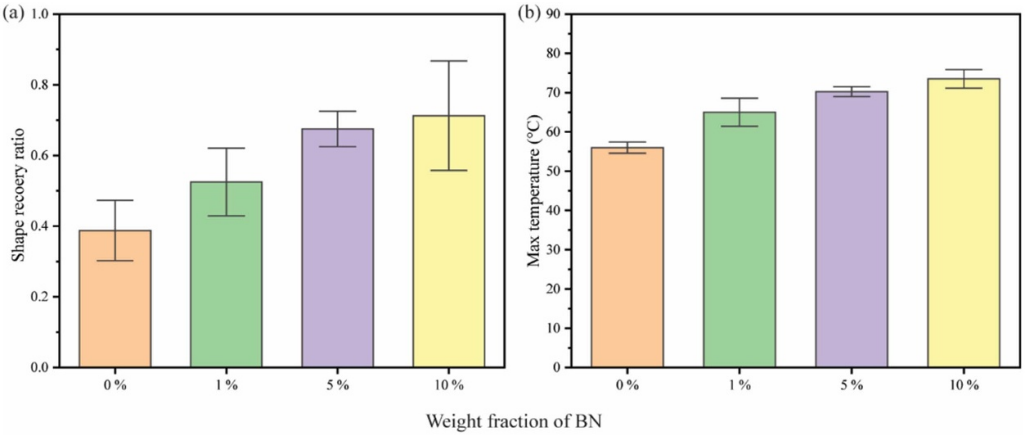

Figure 6. (a) Average variation of shape recovery ratio in each sample with BN weight ratio from 0 to 10%, with error bars showing standard error. (b) Highest temperature in each sample during 5 min of FUS actuation.

applications. Yang *et al* [76] investigated polyurethane composites filled with BN, highlighting its potential in thermal management. They noted that BN's superior thermal conductivity and insulating properties make it an ideal filler for developing thermally insulating polymer composites. Collectively, these studies support the conclusion that BN fillers enhance the thermal response of SMPs under FUS activation, facilitating efficient shape recovery through improved heat generation and distribution.

Overall, to balance shape memory properties with thermal responsiveness and mechanical performance, it is essential to identify optimal BN concentration. In this study, 5 wt.% BN appears to be the optimal concentration, offering a favorable trade-off: it significantly enhances shape recovery while preserving acceptable mechanical strength. This balance makes it a promising formulation for further biomedical applications.

4. Conclusion

Our study successfully demonstrated the production of BN-infused SMPCs with excellent shape recovery qualities following FUS activation. The addition of BN greatly enhanced the thermal conductivity of the SMP matrix, resulting in faster and more efficient shape recovery. The incorporation of 10 wt.% BN significantly enhanced the shape recovery ratio, reaching 75%. This remarkable improvement highlights the potential of BN fillers in optimizing FUS-triggered actuation, particularly beneficial for biomedical applications requiring rapid, precise, and minimally invasive interventions, such as drug-delivery systems, deployable biomedical devices, and smart implants. Comprehensive analyses revealed that BN incorporation reduces crosslinking density and stiffness due to steric hindrance and disrupted curing processes. These effects were evident in the decreased Young's modulus and T_g observed in DMA and tensile testing. Despite these trade-offs, the enhanced viscoelasticity and thermal responsiveness of BN-filled composites make them highly suitable for applications requiring flexibility, precision, and rapid thermal response. Moreover, given the intended biomedical use, future research will include systematic evaluations of biocompatibility and biological properties (such as cytotoxicity, hemocompatibility, and inflammatory response) alongside optimization of BN content and filler dispersion strategies to balance mechanical properties with clinical safety and functionality.

Data availability statement

All data that support the findings of this study are included within the article (and any supplementary files).

Acknowledgment

This work was supported by the US National Science Foundation (NSF) under the Grant, Award No. CMMI 2016474, which is gratefully acknowledged. This paper is dedicated to the memory of Professor Reza Mirzaeifar, from Virginia Tech, passed away on 19 October 2022.

References

[1] Zhao Y, Peng K, Xi J, Shahab S and Mirzaeifar R 2022 Achieving multimodal locomotion by a crosslinked poly(ethylene-co-vinyl acetate)-based two-way shape memory polymer *Smart Mater. Struct.* **31** 015034
[2] Basak S and Bandyopadhyay A 2021 Solvent responsive shape memory polymers-evolution, current status, and future outlook *Macromol. Chem. Phys.* **222** 2100195
[3] Yang S, He Y and Leng J 2022 Shape memory poly (ether ether ketone)s with tunable chain stiffness, mechanical strength and high transition temperatures *Int. J. Smart. Nano Mater.* **13** 1–16
[4] Kulkarni H, Xi J, Sallam A, Lee P, Safranski D, Mirzaeifar R and Shahab S 2024 4D printed shape memory polymers in focused ultrasound fields *Addit. Manuf.* **94** 104465
[5] Xi J, Agrawal A, Shahab S and Mirzaeifar R 2024 Investigation of thermomechanical behaviors of acrylate-based shape memory polymers by molecular dynamics simulation *Polymer* **309** 127445

[6] Xi J, Shahab S and Mirzaeifar R 2022 Qualifying the contribution of fiber diameter on the acrylate-based electrospun shape memory polymer nano/microfiber properties *RSC Adv.* **12** 29162–9

[7] Xing S-T, Wang P-P, Liu S-Q, Xu Y-H, Zheng R-M, Deng Z-F, Peng Z-F, Li J-Y, Wu Y-Y and Liu L 2020 A shape-memory soft actuator integrated with reversible electric/moisture actuating and strain sensing *Compos. Sci. Technol.* **193** 108133

[8] Song L, Hu W, Wang G, Niu G, Zhang H, Cao H, Wang K, Yang H and Zhu S 2010 Tailored (meth)acrylate shape-memory polymer networks for ophthalmic applications *Macromol. Biosci.* **10** 1194–202

[9] Rokaya D, Skallevold H E, Srimaneepong V, Marya A, Shah P K, Khurshid Z, Zafar M S and Sapkota J 2023 Shape memory polymeric materials for biomedical applications: an update *J. Compos. Sci.* **7** 24

[10] Appiah C, Arndt C, Siemsen K, Heitmann A, Staubitz A and Selhuber-Unkel C 2019 Living materials herald a new era in soft robotics *Adv. Mater.* **31** 1807747

[11] Ze Q, Kuang X, Wu S, Wong J, Montgomery S M, Zhang R, Kovitz J M, Yang F, Qi H J and Zhao R 2020 Magnetic shape memory polymers with integrated multifunctional shape manipulation *Adv. Mater.* **32** 1906657

[12] Li C, Zhang S, Jiang J, Wang S, He S and Song J 2024 Laser-induced adhesives with excellent adhesion enhancement and reduction capabilities for transfer printing of microchips *Sci. Adv.* **10** eads9226

[13] Kim J, Son C, Lee S and Kim S 2024 A single microtip shape memory polymer surface with reversible dry adhesion for transfer printing *Adv. Mater. Technol.* **9** 2301468

[14] Huang Y, Zheng N, Cheng Z, Chen Y, Lu B, Xie T and Feng X 2016 Direct laser writing-based programmable transfer printing via bioinspired shape memory reversible adhesive *ACS Appl. Mater. Interfaces* **8** 35628–33

[15] Luo H, Li C, Wang S, Zhang S and Song J 2024 Switchable adhesive based on shape memory polymer with micropillars of different heights for laser-driven noncontact transfer printing *ACS Appl. Mater. Interfaces* **16** 9443–52

[16] Zare M, Davoodi P and Ramakrishna S 2021 Electrospun shape memory polymer micro-/nanofibers and tailoring their roles for biomedical applications *Nanomaterials* **11** 933

[17] Rošic R, Kocbek P, Baumgartner S and Kristl J 2011 Electro-spun hydroxyethyl cellulose nanofibers: the relationship between structure and process *J. Drug Deliv. Sci. Technol.* **21** 229–36

[18] Huang Y *et al* 2025 3D-printed thermally activated shape memory PLA/TBC composite scaffold with body-compatible temperature for minimally invasive bone repair *ACS Appl. Polym. Mater.* **7** 4572–83

[19] Shuai C, Wang Z, Yang F, Zhang H, Liu J and Feng P 2024 Laser additive manufacturing of shape memory biopolymer bone scaffold: 3D conductive network construction and electrically driven mechanism *J. Adv. Res.* **65** 167–81

[20] Small W T, Singhal P, Wilson T S and Maitland D J 2010 Biomedical applications of thermally activated shape memory polymers *J. Mater. Chem.* **20** 3356–66

[21] Guo W *et al* 2025 3D-printed PLA/PEG bone scaffold: body-adaptive thermally responsive shape memory and enhanced biological performance *Surf. Interfaces* **56** 105712

[22] Yang F, He H, Jia J, Wu P, Feng P and Shuai C 2025 Composition and layered co-continuous structure co-regulate shape memory properties *Int. J. Mech. Sci.* **291–2** 110187

[23] Feng P, Yang F, Jia J, Zhang J, Tan W and Shuai C 2024 Mechanism and manufacturing of 4D printing: derived and beyond the combination of 3D printing and shape memory material *Int. J. Extrem. Manuf.* **6** 062011

[24] Wang C, Wang M, Ying S and Gu J 2020 Fast chemo-responsive shape memory of stretchable polymer nanocomposite aerogels fabricated by one-step method *Macromol. Mater. Eng.* **305** 1900602

[25] Gopinath S, Adarsh N N, Nair P R and Mathew S 2023 Recent trends in thermo-responsive elastomeric shape memory polymer nanocomposites *Polym. Compos.* **44** 4433–58

[26] Yang S, He Y and Leng J 2023 Regulated photo/thermal dual and programmable staged responsive shape memory poly(aryl ether ketone) *J. Appl. Polym. Sci.* **140** e54444

[27] Wang F, Jiang M, Pan Y, Lu Y, Xu W and Zhou Y 2023 3D printing photo-induced lignin nanotubes/polyurethane shape memory composite *Polym. Test.* **119** 107934

[28] Huang W, Zhao Y, Wang C, Ding Z, Purnawali H, Tang C and Zhang J 2012 Thermo/chemo-responsive shape memory effect in polymers: a sketch of working mechanisms, fundamentals and optimization *J. Polym. Res.* **19** 1–34

[29] Li G, Fei G, Xia H, Han J and Zhao Y 2012 Spatial and temporal control of shape memory polymers and simultaneous drug release using high intensity focused ultrasound *J. Mater. Chem.* **22** 7692–6

[30] Bhargava A, Peng K and Shahab S 2019 Dynamics of focused ultrasound actuated shape memory polymers *Proc. SPIE* **10967** 1096720

[31] Bhargava A, Peng K, Stieg J, Mirzaeifar R and Shahab S 2017 Ultrasound actuation of shape-memory polymer filaments: acoustic-thermoelastic modeling and testing *ASME 2017 Conf. on Smart Materials, Adaptive Structures and Intelligent Systems*

[32] Bhargava A, Peng K, Mirzaeifar R and Shahab S 2018 Ultrasound actuated shape-memory polymer based drug delivery containers *Proc. SPIE* **10595** 105952H

[33] Delaey J, Dubruel P and Van Vlierberghe S 2020 Shape-memory polymers for biomedical applications *Adv. Funct. Mater.* **30** 1909047

[34] Smith K E, Garcia M, Dupont K M, Higgs G B, Gall K and Safranski D L 2017 Shape-memory polymers for orthopaedic soft-tissue repair *Tech. Orthop.* **32** 141–8

[35] Ramaraju H, Akman R E, Safranski D L and Hollister S J 2020 Designing biodegradable shape memory polymers for tissue repair *Adv. Funct. Mater.* **30** 2002014

[36] Bhargava A and Shahab S 2019 Coupling of nonlinear shape memory polymer cantilever dynamics with focused ultrasound field *Smart Mater. Struct.* **28** 055002

[37] Bhargava A, Peng K, Stieg J, Mirzaeifar R and Shahab S 2017 Focused ultrasound actuation of shape memory polymers; acoustic-thermoelastic modeling and testing *RSC Adv.* **7** 45452–69

[38] Gall K, Yakacki C M, Liu Y, Shandas R, Willett N and Anseth K S 2005 Thermomechanics of the shape memory effect in polymers for biomedical applications *J. Biomed. Mater. Res. A* **73A** 339–48

[39] Yakacki C M, Shandas R, Lanning C, Rech B, Eckstein A and Gall K 2007 Unconstrained recovery characterization of shape-memory polymer networks for cardiovascular applications *Biomaterials* **28** 2255–63

[40] Xi J, Sallam A, Safranski D L, Mirzaeifar R and Shahab S 2024 Hydrophilic and hydrophobic shape memory polymer networks in high-intensity focused ultrasound fields *Smart Mater. Struct.* **33** 025024

[41] Peng K, Zhao Y, Shahab S and Mirzaeifar R 2020 Ductile shape-memory polymer composite with enhanced shape recovery ability *ACS Appl. Mater. Interfaces* **12** 58295–300

[42] Lei M, Chen Z, Lu H and Yu K 2019 Recent progress in shape memory polymer composites: methods, properties, applications and prospects *Nanotechnol. Rev.* **8** 327–51

[43] Amini M, Hasheminejad K and Montazeri A 2020 Experimentally guided MD simulation to enhance the shape memory behavior of polymer-based nanocomposites: towards elaborating the underlying mechanism *Composites A* **138** 106055
[44] Yu J, Xia H, Teramoto A and Ni Q Q 2018 The effect of hydroxyapatite nanoparticles on mechanical behavior and biological performance of porous shape memory polyurethane scaffolds *J. Biomed. Mater. Res. A* **106** 244–54
[45] Jian W, Wang X, Lu H and Lau D 2021 Molecular dynamics simulations of thermodynamics and shape memory effect in CNT-epoxy nanocomposites *Compos. Sci. Technol.* **211** 108849
[46] Zhang H *et al* 2023 4D printing of shape memory polymer nanocomposites for enhanced performances and tunable response behavior *Eur. Polym. J.* **201** 112568
[47] Chen L, Li W, Liu Y and Leng J 2016 Nanocomposites of epoxy-based shape memory polymer and thermally reduced graphite oxide: mechanical, thermal and shape memory characterizations *Composites B* **91** 75–82
[48] Li Y, Lian H, Hu Y, Chang W, Cui X and Liu Y 2016 Enhancement in mechanical and shape memory properties for liquid crystalline polyurethane strengthened by graphene oxide *Polymers* **8** 236
[49] Qu M, Wang H, Chen Q, Wu L, Tang P, Fan M, Guo Y, Fan H and Bin Y 2022 A thermally-electrically double-responsive polycaprolactone—thermoplastic polyurethane/multi-walled carbon nanotube fiber assisted with highly effective shape memory and strain sensing performance *Chem. Eng. J.* **427** 131648
[50] Jo I, Pettes M T, Kim J, Watanabe K, Taniguchi T, Yao Z and Shi L 2013 Thermal conductivity and phonon transport in suspended few-layer hexagonal boron nitride *Nano Lett.* **13** 550–4
[51] Lindsay L and Broido D A 2011 Enhanced thermal conductivity and isotope effect in single-layer hexagonal boron nitride *Phys. Rev. B* **84** 155421
[52] Merlo A, Mokkapati V R S S, Pandit S and Mijakovic I 2018 Boron nitride nanomaterials: biocompatibility and bio-applications *Biomater. Sci.* **6** 2298–311
[53] Çal T and Bucurgat Ü 2019 In vitro investigation of the effects of boron nitride nanotubes and curcumin on DNA damage *DARU J. Pharm. Sci.* **27** 203–18
[54] Lahiri D, Singh V, Benaduce A P, Seal S, Kos L and Agarwal A 2011 Boron nitride nanotube reinforced hydroxyapatite composite: mechanical and tribological performance and *in-vitro* biocompatibility to osteoblasts *J. Mech. Behav. Biomed. Mater.* **4** 44–56
[55] Wang C, Long Y, Deng Y, Han Y, Tishkevich D, Ha M N and Weng Q 2024 Hexagonal boron nitride nanomaterials for biomedical applications *BMEMat* **2** e12068
[56] Liu C and Mather P T 2004 A shape memory polymer with improved shape recovery *MRS Online Proc. Lib.* **855** 112–7
[57] Ostrovskiy S D, Krotenko I A, Stepashkin A A, Zadorozhnyy M Y, Kiselev D A, Ilina T S, Kolesnikov E A and Senatov F S 2023 Shape memory effect and thermal conductivity of PLA/h-BN composites *Polym. Compos.* **44** 7170–80
[58] Standard A.S.T.M 2012 ASTM D4065: standard practice for plastics: dynamic mechanical properties: determination and report of procedures
[59] ASTM Subcommittee D20 1998 *Standard Test Method for Tensile Properties of Plastics* (American Society for Testing and Materials)
[60] Standard, A., D3039/D3039M–08 2008 *Standard Test Method for Tensile Properties of Polymer Matrix Composite Materials* (ASTM International)
[61] Flory P J and Rehner J Jr 1943 Statistical mechanics of cross-linked polymer networks II. Swelling *J. Chem. Phys.* **11** 521–6
[62] ASTM 2008 *F2214-02 (2008): Standard Test Method for In Situ Determination of Network Parameters of Crosslinked Ultra High Molecular Weight Polyethylene (UHMWPE)* (American Society for Testing and Materials) pp 1–5
[63] kinovea 2023 Kinovea (available at: www.kinovea.org)
[64] Zhi C, Bando Y, Tang C, Kuwahara H and Golberg D 2009 Large-scale fabrication of boron nitride nanosheets and their utilization in polymeric composites with improved thermal and mechanical properties *Adv. Mater.* **21** 2889–93
[65] Sui Y, Cui Y, Meng X and Zhou Q 2022 Research progress on the correlation between properties of nanoparticles and their dispersion states in polymer matrix *J. Appl. Polym. Sci.* **139** 52096
[66] Hiremath A, Murthy A A, Thipperudrappa S and Bharath K N 2021 Nanoparticles filled polymer nanocomposites: a technological review *Cogent Eng.* **8** 1991229
[67] Kim M, Jang S, Choi S, Yang J, Kim J and Choi D 2021 Analysis of shape memory behavior and mechanical properties of shape memory polymer composites using thermal conductive fillers *Micromachines* **12** 1107
[68] Pfau M R and Grunlan M A 2021 Smart scaffolds: shape memory polymers (SMPs) in tissue engineering *J. Mater. Chem. B* **9** 4287–97
[69] Asmussen E and Peutzfeldt A 2001 Influence of selected components on crosslink density in polymer structures *Eur. J. Oral Sci.* **109** 282–5
[70] Lyons B J 1983 The effect of radiation on the solubility and other properties of high and linear low density polyethylenes *Radiat. Phys. Chem.* **22** 135–53
[71] Kim D Y, Park J W, Lee D Y and Seo K H 2020 Correlation between the crosslink characteristics and mechanical properties of natural rubber compound via accelerators and reinforcement *Polymers* **12** 9
[72] Liu B, Xia H, Fei G, Li G and Fan W 2013 High-intensity focused ultrasound-induced thermal effect for solid polymer materials *Macromol. Chem. Phys.* **214** 2519–27
[73] Leng J, Lan X, Liu Y and Du S 2011 Shape-memory polymers and their composites: stimulus methods and applications *Prog. Mater. Sci.* **56** 1077–135
[74] Systems F 2023 Limitations of IR thermography in wet and submerged environments *Technical white paper*
[75] Rybak A, Malinowski L, Adamus-Wlodarczyk A and Ulanski P 2021 Thermally conductive shape memory polymer composites filled with boron nitride for heat management in electrical insulation *Polymers* **13** 2191
[76] Yang X, Zhang J, Xia L, Xu J, Sun X, Zhang C and Liu X 2023 Boron nitride/polyurethane composites with good thermal conductivity and flexibility *Int. J. Mol. Sci.* **24** 8221